Multipole expansion solution of the Laplace equation using surface data

Shashikant Manikonda*, Martin Berz

Department of Physics and Astronomy, Michigan State University, East Lansing, MI 48823, USA

Available online 1 December 2005

Abstract

This paper provides a computational method to model a three-dimensional static electromagnetic field within a finite source free volume starting from discrete field information on its surface. The method uses the Helmholtz vector decomposition theorem and the differential algebraic framework of COSY INFINITY to determine a solution to the Laplace equation. The solution is locally expressed as a Taylor expansion of the field which can be computed to arbitrary order. It provides a natural multipole decomposition of the field which is required for the computation of transfer maps, and also allows to obtain very accurate finite element representations with very small numbers of cells.
© 2005 Elsevier B.V. All rights reserved.

PACS: 41.20.Gz; 41.20.Cv

Keywords: Laplace equation; COSY Infinity; Helmholtz vector decomposition theorem; Differential algebra; Multipole expansion; Surface data

1. Introduction

The detailed simulation of particle trajectories through magnets in spectrographs and other large acceptance devices requires the use of detailed field information obtained from measurements. Likewise, for high-energy accelerators like the LHC, higher order description of the beam dynamic via one-turn maps is required to study the long-term beam stability [1,2]. The construction of such high-order one-turn truncated Taylor maps [3] requires the precise information of the electromagnetic field in the individual electromagnetic components (quadrupoles, dipole, sextupoles, etc.) of the lattice.

It is commonly known that for a device that satisfies mid-plane symmetry, the entire field information can be extracted from the data in the mid-plane of the device [3]. However, it is well known that this method has limitations in accurately predicting nonlinear field information outside the immediate vicinity of the mid-plane because the extrapolation requires the computation of higher order derivatives of in-mid-plane data, which is difficult to do with accuracy if the data is based on measurements. Thus, it is particularly useful to employ techniques that rely on field measurements outside the mid-plane. In particular, in modern particle spectrographs it is common to measure the fields on a fine mesh on 2–4 planes outside the mid-plane. These data have frequently been used to model the overall field as a superposition of point-charge fields of so-called image charges [4,5]. However, the computational effort required for this approach is large, as it requires the inversion of a matrix with a dimension equal to that of the number of image charges.

However, the out-of-plane field measurements in essence provide field data on the top and bottom surfaces of a box containing the region of interest through which the beam passes. If the planes extend outward far enough to a region where the fringe field becomes very small, or can easily be modeled, and inwards far enough that the field becomes rather homogenous, field data are known on an entire surface enclosing the region of interest. The method we present in this paper can extract the field information as a multipole expansion in the volume of interest if a discrete set of field measurements are provided on a closed surface enclosing the volume of interest.

---
*Corresponding author. Tel.: +1 517 355 9200; fax: +1 360 294 3258.

E-mail addresses: manikond@msu.edu (S. Manikonda), berz@msu.edu (M. Berz).

Thus, the field computation problem can be viewed as solving a boundary value problem for the three-dimensional (3D) Laplace equation for the field, i.e. to obtain the solution of the PDE

$$\nabla^2 \psi(\vec{r}) = 0 \quad \text{in the volume } \Omega \subset \mathbb{R}^3$$

where $\nabla \psi(\vec{r}) = \vec{f}(\vec{r})$ is specified on the surface $\partial \Omega$.

The existence and uniqueness of the solution for the 3D case can easily be shown through the application of Green's formulae. In particular, it is well known that the component of $\vec{\nabla}\psi$ normal to the surface is sufficient to specify the solution; however, in the following we will also make use of the additional field components available from measurements. It is well known that the analytic closed-form solution for the 3D case can be found for problems with certain regular geometries where a separation of variables can be performed. However, in most practical 3D cases, numerical methods are the only way to proceed. Usually the finite difference or finite element approach are used to find the numerical solution as data set in the region of interest. But because of their relatively low approximation order, for the problem of precise solution of PDEs, the methods have limited success because of the prohibitively large number of mesh points required. The method we present in this paper can determine local finite elements of in principle unlimited order.

In Section 2 we discuss the benefits of using the boundary data and present the analytic closed form solution for the 2D case that can be easily found by application of Cauchy's integral formula. We then use a 2D example to highlight the advantages of the methods that use the boundary data to compute the solution. In Section 3 we present the theory and the implementation of the new scheme to find the solution of the 3D Laplace equation when the gradient of the solution is specified on the surface enclosing the volume of interest . This scheme is based on the Helmholtz theorem and the tools of the code COSY Infinity [3,6,7]. In Section 4 we present an application of this new scheme to a theoretical bar magnet problem. We also address the results of an application to the study of a dipole magnet of the MAGNEX spectrograph.

2. Methods using boundary data

Boundary data methods such as those utilized below are based on a description of the interior field in terms of particular surface integrals involving the surface data. These approaches have various advantages. Firstly, the solution is analytic in terms of the interior variables, even if the boundary data fail to be differentiable or are even piecewise discontinuous; all such non-smoothness is removed after the integration is executed. Hence a Taylor polynomial approximation in terms of interior variables can be performed; and we expect that a Taylor approximation of a certain order will provide an accurate approximation over suitable domains.

Secondly, since for the PDEs under consideration here the solution functions are known to assume their extrema on the boundary because of analyticity or harmonicity, a method that uses boundary data is expected to be robust against errors in those boundary data with errors in the interior not exceeding the errors on the surface. Thirdly, if the boundary data given have statistical errors, such errors have a tendency to even average out in the integration process as long as the contributions of individual pieces of integration are of similar significance. Thus, we expect the error in the computed field in the interior to be generally much smaller than the error in the boundary data. This ensures that the methods using boundary data are computationally stable.

2.1. The 2D case

As an introduction to the general approach, we begin with the discussion of the 2D case, the theory of which can be fully developed in the framework of elementary complex analysis, and which also describes the situation of static electric or magnetic fields as long as no longitudinal field dependence is present. It is based on the use of Cauchy's integral formula stating that if the function f is analytic in a region containing the closed path C, and if α is a point within C, then

$$f(\alpha) = \frac{1}{2\pi i} \oint_C \frac{f(z)}{z - \alpha} \, dz \tag{1}$$

where the integral denotes the path integral over C. Cauchy's formula is an integral representation of f which permits us to compute f anywhere in the interior of C, knowing only the value of f on C. This integral representation of f is also the solution of the 2D Laplace equation for the primitive of $(\text{Re}(f), -\text{Im}(f))$ with the function f specified on the path C.

Now, suppose a random error of $\delta(z)$ is introduced in the measured data around the path C. Then by Eq. (1) we can compute the error $E(a)$ introduced in the computation of $f(\alpha)$ at some point α inside C as

$$E(\alpha) = \frac{1}{2\pi i} \oint_C \frac{f(z) + \delta(z)}{z - \alpha} \, dz - f(\alpha)$$
$$= \frac{1}{2\pi i} \oint_C \frac{\delta(z)}{z - \alpha} \, dz \tag{2}$$

We note that while $E(\alpha)$ is given by a Cauchy integral, E need not be analytic since $\delta(z)$ need not assume the function values of an analytic function. In fact, if it would, then it already would be uniquely specified on any dense subset S of C, which removes the freedom for all values of E on points on C that are not in S.

While the error E itself may be bounded in magnitude, if the integral is approximated by one of the conventional numerical quadrature methods, the result can become singular as the point α approaches the boundary C. This case may limit the practical use of the method and needs to be studied carefully. As an example, we consider the case of

quadrature based on adding the terms of a Riemann sum, i.e. the approximation

$$\frac{1}{2\pi i} \oint_C \frac{\delta(z)}{z-\alpha} \, dz \approx \frac{1}{2\pi i} \sum_{j=1}^{N_z} \frac{\delta(z_j)}{(z_j - \alpha(r))} (z_j - z_{j-1})$$
$$= \tilde{E}(\alpha) \tag{3}$$

where the N_z points z_j are spaced equidistantly around C; since C is closed, $z_0 = z_{N_z}$. By studying the approximation $\tilde{E}(a)$ as the point α approaches the boundary C, we can analyze the stability of the method with respect to the discretization of the path C.

As an example, we choose the path C as a circle of radius R enclosing the region of interest. We assume a random error of $\delta(z)(\pm 10^{-2})$ is introduced in the measured data around C. The point α is given by $r \exp(i\phi)$ and the points z_j are given by $R \exp(i 2\pi j / N_z)$ for $j = 0, \ldots, N_z$. Letting $\delta_m(z_j)$ denote the error assigned to point z_j in error set m, for each of these error sets we express the Riemann sum $\zeta_m(\alpha)$ for point α by

$$\zeta_m(\alpha) = \frac{1}{2\pi i} \sum_{j=1}^{N_z} \frac{i z_j \delta_m(z_j)}{(z_j - \alpha(r))} \frac{2\pi}{N_z}.$$

We then form the average of the magnitude of the error over N_e error sets to obtain

$$\eta(r) = \frac{1}{N_e} \sum_{m=1}^{N_e} |\zeta_m(\alpha)|.$$

Note that $\eta(r)$ still depends on the phase ϕ. However, in the statistical limit there is apparently invariance under rotation by $\exp(i 2\pi / N_z)$; and one quickly sees that there are two limiting cases for the choice of the phase. These are the case $\phi = 0$, where the α will eventually collide with the z_j for $j = N_z$ as $r \to R$ and thus a "worst case" divergence will appear, and the case $\phi = 2\pi / 2N_z$, in which case the α will approach the mid-point between z_j for $j = N_z$ and z_j for $j = 1$ as $r \to R$. Choosing sufficiently fine discretization of the path and sufficiently many error sets δ_m, the quantity $\eta(r)$ for these two cases will be a good measure for the accuracy that can be achieved with the surface integral method.

For our specific example, we choose random errors of maximum magnitude 10^{-2} at $N_z = 10,000$ points on the circle of radius $R = 2$. For each value of r, we perform the computation for a total of $N_e = 10,000$ error sets. The results of this analysis are shown as plots in Figs. 1 and 2 for the two phases that represent the "worst case" and the "best case" situation.

We first observe that sufficiently away from the surface, the expected smoothing effect is happening, and the errors in the function values are indeed well below the errors assumed on the surface. A rough quantitative analysis shows that this error is about two orders of magnitude below the surface data error, corresponding well with the statistically expected decrease of the error by $1/\sqrt{N_z}$. As α approaches the curve closer than 10^{-3}, in the "best case"
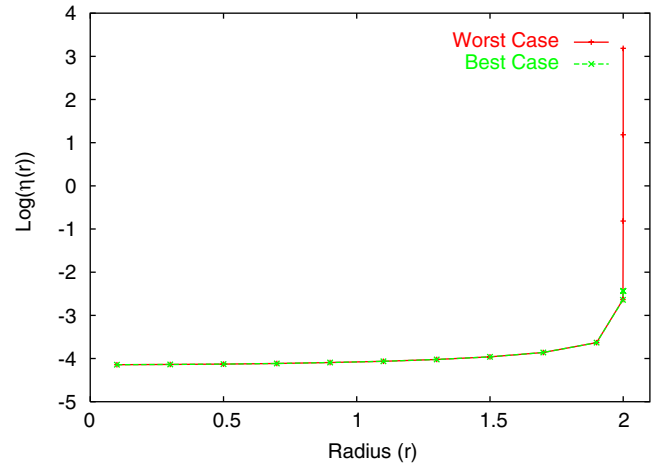

Fig. 1. The plot shows the dependency of $\eta(r)$ on the radius r. The Y-axis represents $\log(\eta(r))$ and the X-axis represents the radius r. Ten thousand error sets (N_e) around the circle or radius $R = 2$ were chosen for the analysis. We show the plot for both the best and the worst case scenario.
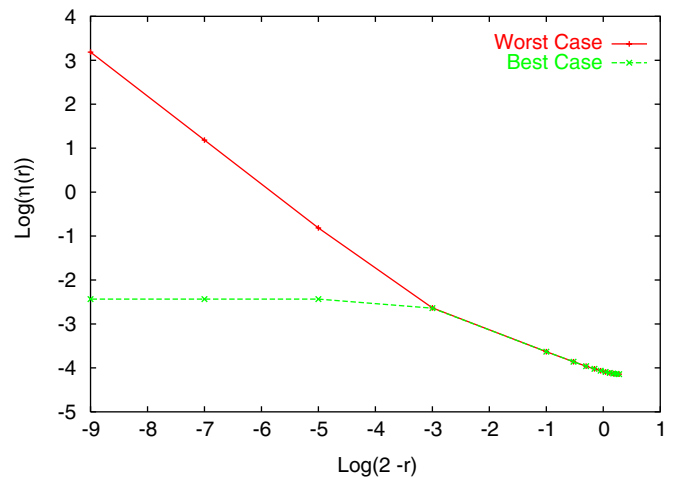

Fig. 2. The plot shows the dependency of $\eta(r)$ on the radius as the radius r approaches the boundary. The Y-axis represents $\log(\eta(r))$ and the X-axis represents $\log(2 - r)$. Ten thousand error sets (N_e) around the circle or radius $R = 2$ were chosen for the analysis. We show the plot for both the best and the worst case scenario.

situation, the error rises to about 10^{-2}, which is because now only nearby grid points contribute to the sum and thus the smoothing effect disappears. In the "worst case" scenario, divergence actually happens; but the average error is still at the level of the original random error of 10^{-2} for values of r that are only about 10^{-4} away from the radius 2.

So overall we see that the method performs significant smoothing, and even with the simplest discretization as a Riemann sum, good accuracy is maintained even as we approach C. We note in passing that with more sophisticated quadrature methods, for example, those based on Gaussian methods [3], the divergence effect can be significantly controlled.

3. The 3D case

The scheme we use for the 3D case is based on the Helmholtz vector decomposition theorem [8–14]. We begin by representing the solution of the PDE via Helmholtz' theorem, which states that any vector field $\vec{B}$ which vanishes at infinity can be written as the sum of two terms, one of which is irrotational and the other solenoidal as

$$\vec{B}(\vec{x}) = \vec{\nabla} \times \vec{A}_t(\vec{x}) + \vec{\nabla}\phi_n(\vec{x}) \tag{4}$$

$$\phi_n(\vec{x}) = \frac{1}{4\pi} \int_{\partial\Omega} \frac{\vec{n}(\vec{x}_s) \times \vec{B}(\vec{x}_s)}{|\vec{x} - \vec{x}_s|}\, ds$$
$$- \frac{1}{4\pi} \int_{\Omega} \frac{\vec{\nabla} \times \vec{B}(\vec{x}_v)}{|\vec{x} - \vec{x}_v|}\, dV$$

$$\vec{A}_t(\vec{x}) = -\frac{1}{4\pi} \int_{\partial\Omega} \frac{\vec{n}(\vec{x}_s) \times \vec{B}(\vec{x}_s)}{|\vec{x} - \vec{x}_s|}\, ds$$
$$+ \frac{1}{4\pi} \int_{\Omega} \frac{\vec{\nabla} \times \vec{B}(\vec{x}_v)}{|\vec{x} - \vec{x}_v|}\, dV.$$

Here $\partial\Omega$ is the surface which bounds the volume Ω. $\vec{x}_s$ denotes a point on the surface $\partial\Omega$, and $\vec{x}_v$ denotes a point within Ω. $\vec{n}$ is the unit vector perpendicular to $\partial\Omega$ that points away from Ω. $\vec{\nabla}$ denotes the gradient with respect to $\vec{x}_v$.

For the special case that $\vec{B} = \vec{\nabla}V$, we have $\vec{\nabla} \times \vec{B} = 0$; furthermore, if V is a solution of the Laplace equation $\vec{\nabla}^2 V = 0$, we have $\vec{\nabla} \cdot \vec{B} = 0$. Thus in this case, all the volume integral terms vanish, and $\phi_n(\vec{x})$ and $\vec{A}_t(\vec{x})$ are completely determined from the normal and the tangential components of $\vec{B}$ on the surface $\partial\Omega$ via

$$\phi_n(\vec{x}) = \frac{1}{4\pi} \int_{\partial\Omega} \frac{\vec{n}(\vec{x}_s) \times \vec{B}(\vec{x}_s)}{|\vec{x} - \vec{x}_s|}\, ds \tag{5}$$

$$\vec{A}_t(\vec{x}) = -\frac{1}{4\pi} \int_{\partial\Omega} \frac{\vec{n}(\vec{x}_s) \times \vec{B}(\vec{x}_s)}{|\vec{x} - \vec{x}_s|}\, ds. \tag{6}$$

For static electric or magnetic fields without sources in Ω, which are characterized by the Laplace problem that we are studying, the divergence and the curl of the field vanish and hence these fields can be decomposed into irrotational and solenoidal parts. For any point within the volume Ω, the scalar and vector potentials depend only on the field on the surface $\partial\Omega$. And due to the smoothing properties of the integral kernel, the interior fields will be analytic even if the field on the surface data fails to be differentiable.

It is worth noting that there are also various higher dimensional extensions to the Helmholtz theorem [15,16] which may be useful to also solve certain 4D boundary value problems.

3.1. Surface integration and finite elements via DA

Since the expressions (5) and (6) are analytic, they can be expanded at least locally. The idea is now to expand them to higher orders in BOTH the two components of the surface variables $\vec{x}_s$ and the three components of the volume variables $\vec{x}$. The polynomial dependence on the surface variables will be integrated over surface sub-cells, which results in a highly accurate integration formula with an error order equal to that of the expansion. The dependence on the volume variables will be retained, which leads to a high-order finite element method. By using sufficiently high order, high accuracy can be achieved with a small number of surface elements, and more importantly, a small number of volume elements. We describe the details of the implementation in the following.

The volume Ω is subdivided into volume elements. Using the prescription for the surface field, the Taylor expansion of the field is computed at the center of each volume element. The final solution inside the overall volume is given as local expansions of the field in different volume elements.

To find the local expansions for each volume element, we first split the domain of integration $\partial\Omega$ into smaller elements Γ_i. From the surface field formula we extract an approximate Taylor expansion in the surface variables $\vec{x}_s$ about the center of the surface element. Then the integral kernel $1/|\vec{r} - \vec{r}_s|$ and the field $\vec{B}$ on the surface are Taylor expanded in the surface variables $\vec{r}_s$ about the center of each surface element. We also Taylor expand the kernel in the volume variables $\vec{r}$ about the center of the volume element. The final step is to integrate and sum the resulting Taylor expansions for all surface elements. Depending on the accuracy of the computation needed we choose step sizes, order of expansion in $r(x, y, z)$, and order of expansion in $r_s(x, y, z)$.

All the mathematical operations to perform the expansion, surface integration, curl and divergence were implemented using the high-order multivariate differential algebraic tools available in the code COSY Infinity [3,6,7] which automatically leads to the respective field representation to any order without any manual computations.

4. Applications

4.1. An analytical example: the bar magnet

As a reference problem we consider the magnetic field of an arrangement of the two rectangular iron bars with inner surfaces ($y = \pm y_0$) parallel to the mid-plane ($y = 0$) as shown in Fig. 3. The interior of these uniformly magnetized bars, which are assumed to be infinitely extended in the $\pm y$-directions is defined by: $x_1 \leqslant x \leqslant x_2$, $|y| \leqslant y_0$, and $z_1 \leqslant z \leqslant z_2$. From this bar magnet one can obtain an analytic solution for the magnetic field $\vec{B}(x, y, z)$—see for example
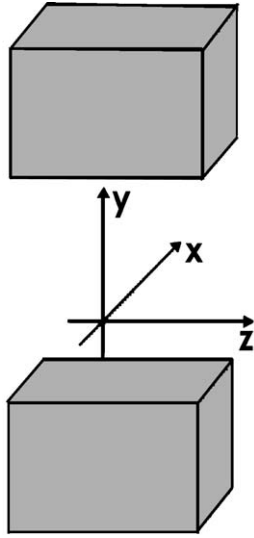
Fig. 3. Geometric layout of the bar magnet, consisting of two bars of magnetized material.

Fig. 4. Magnetic field B_y on the center plane of the bar magnet. $B_0 = 1$ T and the interior of this magnet is defined by $-0.5 \leqslant x \leqslant 0.5$, $|y| \leqslant 0.5$, and $-0.5 \leqslant z \leqslant 0.5$.

Ref. [17]—and the result is given by

$$B_y(x,y,z) = \frac{B_0}{4\pi} \sum_{i,j=1}^{2} (-1)^{i+j}$$
$$\times \left[\arctan\left(\frac{X_i Z_j}{Y_+ R_{ij}^+} \right) + \arctan\left(\frac{X_i Z_j}{Y_- R_{ij}^-} \right) \right]$$

$$B_x(x,y,z) = \frac{B_0}{4\pi} \sum_{i,j=1}^{2} (-1)^{i+j} \left[\ln\left(\frac{Z_j + R_{ij}^-}{Z_j + R_{ij}^+} \right) \right]$$

$$B_z(x,y,z) = \frac{B_0}{4\pi} \sum_{i,j=1}^{2} (-1)^{i+j} \left[\ln\left(\frac{X_j + R_{ij}^-}{X_j + R_{ij}^+} \right) \right]$$

where $X_i = x - x_i$, $Y_\pm = y_0 \pm y$, $Z_i = z - z_i$, and $R_{ij}^\pm = (X_i^2 + Y_j^2 + Z_{\pm}^2)^{1/2}$. We note that because of the symmetry of the field around the mid-plane, only even order terms exist in the Taylor expansion of this field about the origin. The mid-plane field of such a magnet is shown in Fig. 4.

4.1.1. Results and analysis

As a first step, we study the performance of the surface integration method. To this end, the six surfaces are each subdivided into a 44×44 mesh. The entire volume is considered as one volume element, which is characteristic of the situation in which the entire system has to be represented by merely a single multipole expansion. On each of the surface mesh cells, the contribution from the Helmholtz integral is Taylor expanded [3,18], and the resulting polynomial is integrated. Fig. 5 shows the accuracy of the predicted field, compared with the exact solution, as a function of the order of expansion within the surface mesh cells. Results are shown for the points $(0,0,0)$ and $(0.1,0.1,0.1)$. It can be seen that at order six, an
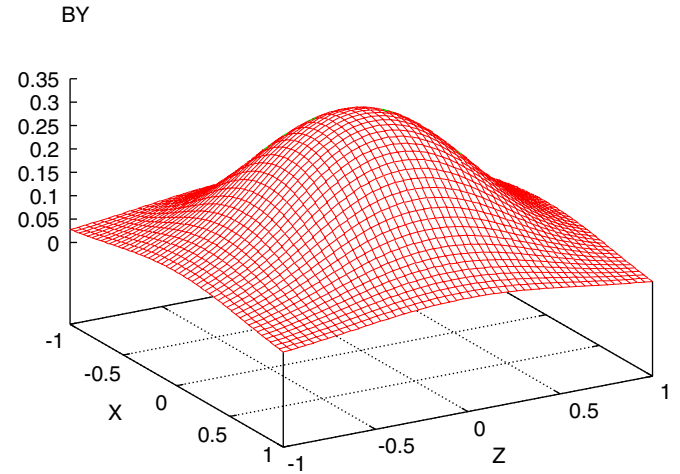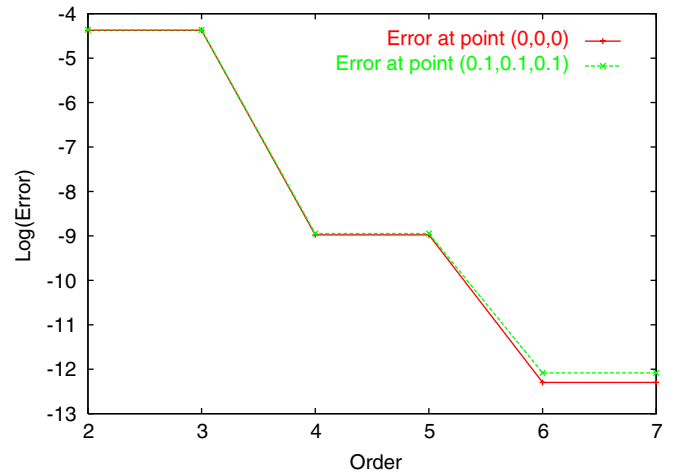

Fig. 5. Error for the field calculated for the bar magnet example for individual points $(0,0,0)$ and $(0.1,0.1,0.1)$.

accuracy of approximately 10^{-12} is reached, which is very high compared to conventional numerical field solvers.

We note that the change from order 2 to 3, 4 to 5 and 6 to 7 do not produce significant change in the error. This is due to the fact that odd order terms do not exist in the Taylor expansion of the field around the reference point $(0,0,0)$.

For the next example, we split the volume inside the bar magnet into $5 \times 5 \times 5$ finite elements of width ± 0.2. Within each of the elements, a Taylor expansion in the three volume variables is carried out, resulting in a polynomial representation of the field within the finite element cell. The polynomial representation is used to evaluate the field at 1000 randomly chosen points within the cell, and comparing the result with the analytical answer. Fig. 6 shows the resulting RMS error for finite elements centered around $(0,0,0)$ and $(0.1,0.1,0.1)$. It can be seen that at order 7, an accuracy of approximately 10^{-6} is reached.

Overall, the method of simultaneous surface and volume expansion that can be carried out automatically with the
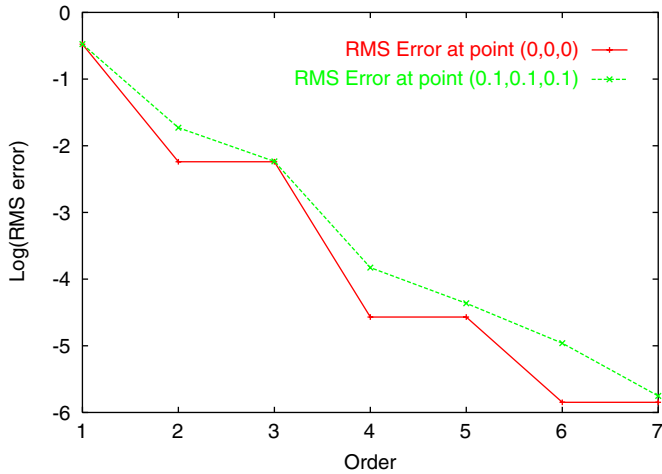
Fig. 6. Average error for the field calculated for the bar magnet example for finite elements of width 0.4 around points $(0,0,0)$ and $(0.1, 0.1, 0.1)$.

expansion in x_s and y_s below, the entries in the first column provide the number assigned to each of the coefficients in the Taylor expansion to easily identify them. The entries in the second column provide the numerical value of the coefficients. The entries in the fourth, fifth and the sixth columns provide the expansion orders with respect to the volume variables (x, y, z). And the entries in the seventh and eighth column provide the expansion orders with respect to the surface variables (x_s, y_s). The total order for each coefficient is the sum of all the orders in columns four through eight, which is given in the third column. Since we compute the Taylor expansion about a particular point $(0.1, 0.1, 0.1)$ frozen in the volume of interest in two surface variables (x_s, y_s), we notice that the entries in column four, five, six are all zero. It can be seen that in this expansion, the contributions of higher order terms depending on the surface variables decrease rapidly, and thus the expansion shown would lead to a result of very high accuracy.

Sample eighth order Taylor expansion in two surface variables

I	Coefficient	Order	Exponents				
1	0.1430015055365947E-01	0	0	0	0	0	0
2	0.6922600731781813E-03	1	0	0	0	1	0
3	-0.9437452710153340E-03	1	0	0	0	0	1
4	-0.1561210105220474E-04	2	0	0	0	2	0
5	-0.4471499751575185E-04	2	0	0	0	1	1
⋮							
20	-0.3232493054085583E-07	5	0	0	0	1	4
21	0.6156849473575023E-07	5	0	0	0	0	5
22	0.8960505971632865E-10	6	0	0	0	6	0
23	0.1890553337467643E-08	6	0	0	0	5	1
24	-0.9792219471281489E-09	6	0	0	0	4	2
⋮							
41	-0.2417698920592542E-10	8	0	0	0	4	4
42	0.7717865536738434E-10	8	0	0	0	3	5
43	-0.2649803372019223E-11	8	0	0	0	2	6
44	-0.2561415687161454E-10	8	0	0	0	1	7
45	0.8506329051477273E-10	8	0	0	0	0	8

tools in the code COSY Infinity [3,6,7,18] leads to accuracies that are significantly higher than those of conventional finite element tools, even when unusually large finite elements are used.

For purposes of illustration, we now show the Taylor expansion of the field given by Eq. (5) and calculated using the DA tools of COSY over one surface element for a particular point frozen inside the volume of interest. The center of the surface element is at $(-0.39, -0.39, 0.5)$ and the point is at $(0.1, 0.1, 0.1)$. The surface element is described by $(-0.39 + 0.5\lambda_x x_s, -0.39 + 0.5\lambda_y y_s, 0.5)$, where λ_x, λ_y represent the length and width of the surface element and $x_s, y_s \in [-1, 1]$. In the representation of the Taylor

We now present the Taylor expansion of the contribution of (5) for one surface element and over one volume element inside the volume of interest. The center of the surface element is at $(-0.39, -0.39, 0.5)$ and the center of the volume element is at $(0.1, 0.1, 0.1)$. The surface element and the volume element can be fully described by $(-0.39 + 0.5\lambda_x x_s, -0.39 + 0.5\lambda_y y_s, 0.5)$ and $(0.1 + 0.5\rho_x x, 0.1 + 0.5\rho_y y, 0.1 + 0.5\rho_z z)$, respectively, where λ_x, λ_y represent the length and width of the surface element, and ρ_x, ρ_y, ρ_z represent the length, width and height of the volume element, and $x_s, y_s, x, y, z \in [-1, 1]$. In this case the coefficients of the Taylor expansion depend on both the surface (x_s, y_s) and the volume variables (x, y, z). The coefficients

depending only on the surface variables and the coefficient of the zeroth order term are same as in the previous example of the expansion in just the surface variables. Once again we notice that the contributions of higher order terms decrease rapidly for higher order, showing that also the expansion in volume variables leads to a very accurate representation.

dependence of the average error on the length of the volume element and the total number of volume elements. As an example, for cell lengths of 0.1, which leads to a total number of only 550 finite elements, an accuracy of 10^{-10} can be reached with a ninth order method. Similarly, for a seventh order method with a cell length of 0.2, corresponding to 125 boxes, accuracies of about 10^{-6} can be reached.

Sample eighth order Taylor expansion in two surface variable and three volume variables

I	Coefficient	Order	Exponents				
1	0.1430015055365947E-01	0	0	0	0	0	0
2	-0.9590481459719686E-02	1	1	0	0	0	0
3	-0.9590481459719686E-02	1	0	1	0	0	0
4	-0.9768082968233012E-02	1	0	0	1	0	0
5	0.6922600731781813E-03	1	0	0	0	1	0
6	-0.9437452710153340E-03	1	0	0	0	0	1
⋮							
454	-0.4509222359486833E-07	6	0	1	0	0	5
455	-0.3067430813781439E-07	6	0	0	1	0	5
456	0.8960505971632865E-10	6	0	0	0	6	0
457	0.1890553337467643E-08	6	0	0	0	5	1
458	-0.9792219471281489E-09	6	0	0	0	4	2
⋮							
1283	-0.2417698920592547E-10	8	0	0	0	4	4
1284	0.7717865536738462E-10	8	0	0	0	3	5
1285	-0.2649803372019148E-11	8	0	0	0	2	6
1286	-0.2561415687161455E-10	8	0	0	0	1	7
1287	0.8506329051477271E-10	8	0	0	0	0	8

We now study the error dependency on the size (length) of the volume element, or equivalently the number of volume elements chosen for the computation. For the order of computation 3,5,7 and 9, Figs. 7 and 8 provide the

Compared to conventional 3D Laplace solvers which typically utilize in the order of 10^6 cells to achieve accuracies in the order of 10^{-3}, these results are quite promising.
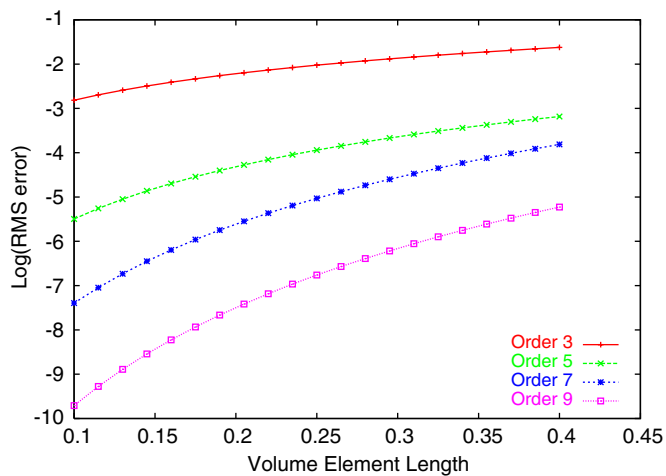

Fig. 7. The plot shows the dependency of the average error on the length of the volume element.
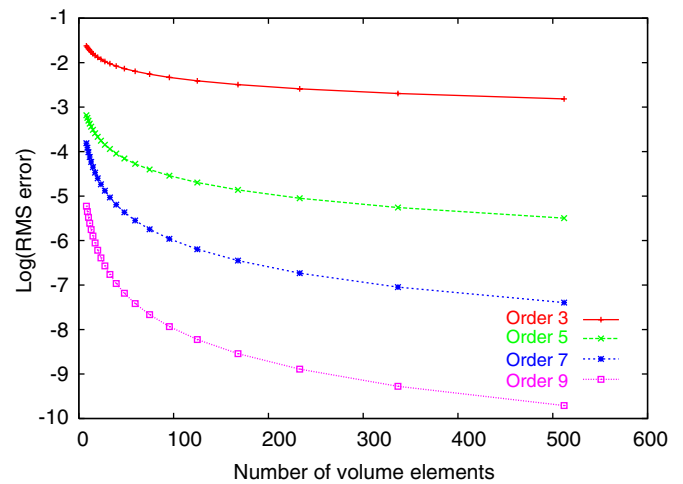

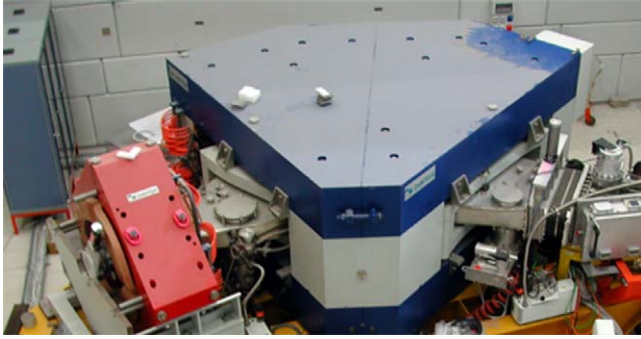Fig. 8. The plot shows the dependency of the average error on the number of volume element.

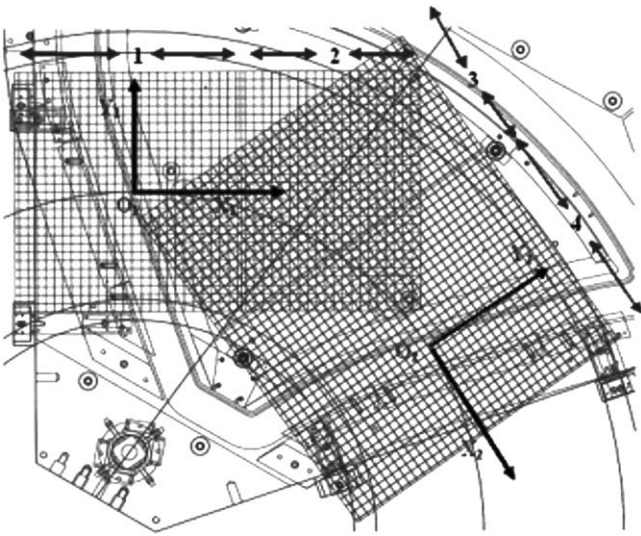Fig. 9. The dipole magnet of the MAGNEX spectrometer; courtesy A. Cunsolo.

Fig. 10. Layout of the measurement grids in different regions of the dipole magnet. Courtesy A. Lazzaro.

4.2. The dipole magnet of the MAGNEX spectrometer

We now address a practical application of this method to magnetic spectrometers. The trajectory reconstruction method [19] is one of the important tools to study magnetic spectrometers. Good computational modeling of the dipole magnet is very important for this tool to work, and this is particularly so for modern large-aperture devices such as MAGNEX at INFN, Catania, Italy [20–22]. Fig. 9 shows the MAGNEX spectrometer configuration.

As mentioned above, for purposes of measurement economy, magnet builders usually provide the magnetic field only on few separate horizontal planes within the dipole, while the computational treatment of the device requires the knowledge of the field in all of space. The MAGNEX dipole was divided into a number of volumes defined by areas and planes as shown in Fig. 10. Four areas were mapped as indicated in Table 1; areas 1 and 4 comprise the effective field boundary regions of the magnet at the entrance and at the exit where the field undergoes a sudden variation due to the fringe field effects, whereas

Table 1
Areas mapped in the dipole

Area	
1	EFB area at entrance
2	Central area entrance end
3	Central area exit end
4	EFB area at exit

Table 2
Planes mapped in the dipole

Planes	$\mathbf{Z}$ (cm)	
a	0	Mid-plane
b	1.6	Above mid-plane
c	3.2	Above mid-plane
d	4.8	Above mid-plane
e	6.4	Above mid-plane
f	8.0	Above mid-plane
g	−4.8	Below mid-plane

regions 2 and 3 represent the central region of the magnet. This subdivision is the result of the need of different grid sizes over the mapped area in order to limit the measurement time. For each of the regions, the measurements were taken on seven different planes as shown in Table 2.

The magnetic measurement were organized so that the RMS error $\langle \Delta B_i / B \rangle$ $i = x, y, z$ at any mesh point inside the working volume of the magnet was not greater than 5×10^{-4}. The field measurement error due to the error of measuring the Hall probe voltage was $\Delta B = \pm 5 \times 10^{-5}$ G. The main source of the B measurement error were assumed to be the errors of positioning the Hall probe [23–25].

Utilizing that sufficiently outside the dipole the fields will vanish, it is thus possible to provide field data over the surface of a finite box enclosing the region of interest, and thus to apply the methods described above to obtain a field representation everywhere. We use this method to compute the fields in region 1 and plane A of the dipole magnet. The contour plot of the resulting relative errors is plotted over region 1 in Fig. 11. The region where the sharp valley is observed coincides with the physical boundary of the dipole magnet.

5. Conclusion

A new technique for finding the multipole expansion solution of the 3D Laplace equation using surface data has been developed. Since this new technique uses the field information on the surface enclosing the volume of interest and is implemented using the high-order multivariate differential algebraic tools available in the code COSY Infinity [3,6,7], the accuracy achieved is much higher than that of conventional field solvers. If the data on the surface
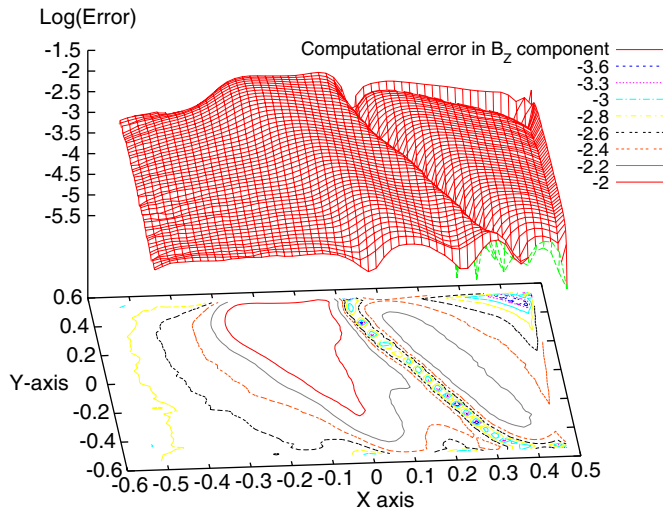
Fig. 11. Contour plot of the magnetic field errors for region 1 and plane A.

enclosing the volume of interest can be given exactly, then in principle arbitrarily high accuracy limited only by the computational resources available can be achieved by this new technique. In practical situations where the field data on the surface enclosing the volume of interest is experimentally measured, the discretization of the surface and the errors in the experimentally measured field data may limit the accuracy achieved, but because the method is naturally smoothing, the accuracy is expected to exceed that of the measurements. The use of this new technique has been tested rather successfully for an analytic example of the bar magnet. The result from a preliminary analysis of the data from the MAGNEX spectrograph dipole magnet is also presented.

Acknowledgements

References

[1] M.L. Shashikant, M. Berz, B. Erdélyi, COSY INFINITY's EXPO symplectic tracking for LHC, IOP CP, vol. 175, 2004, pp. 299–306.

[2] B. Erdélyi, M. Berz, K. Makino, Detailed analysis of fringe field effects in the large hadron collider, Technical Report MSUCL-1129, National Superconducting Cyclotron Laboratory, Michigan State University, East Lansing, MI 48824, 1999.

[3] M. Berz, Modern Map Methods in Particle Beam Physics, Academic Press, San Diego, 1999 and Also available at ⟨http://bt.pa.msu.edu/pub⟩.

[4] R. Degenhardt, M. Berz, Nucl. Instr. and Meth. A 427 (1999) 151.

[5] M. Berz, B. Fawley, K. Hahn, Nucl. Instr. and Meth. A 307 (1991) 1.

[6] M. Berz, K. Makino, COSY INFINITY Version 8.1—user's guide and reference manual, Technical Report MSUHEP-20704, Department of Physics and Astronomy, Michigan State University, East Lansing, MI 48824, 2002, see also ⟨http://cosy.pa.msu.edu⟩.

[7] M. Berz, J. Hoefkens, K. Makino, COSY INFINITY Version 8.1—programming manual, Technical Report MSUHEP-20703, Department of Physics and Astronomy, Michigan State University, East Lansing, MI 48824, 2002. see also ⟨http://cosy.pa.msu.edu⟩.

[8] H.v. Helmholtz, J. Reine Angew. Math. Crelle's J. 55 (1858) 25.

[9] P.M. Morse, H. Feshbach, Meth. Theor. Phys. Part I and II, (1953).

[10] P.L. Walstrom, Nucl. Instr. and Meth. A 519 (1–2) (2004) 216.

[11] M. Venturini, A.J. Dragt, Nucl. Instr. and Meth. A 427 (1999) 387.

[12] M. Venturini, A. Dragt, Computing transfer maps from magnetic field data, in: IEEE Particle Accelerator Physics Conference, 1999.

[13] M. Venturini, D. Abell, A. Dragt, Map computation from magnetic field data and application to the lhc high-gradient quadrupoles, eConf C980914, 1998, pp. 184–188.

[14] P. Walstrom, A. Dragt, T. Stasevich, Computation of charged-particle transfer maps for general fields and geometries using electromagnetic boundary-value data, in: IEEE Particle Accelerator Conference 2001, 2001.

[15] D.A. Woodside, J. Math. Phys. 41 (7) (2000) 4622.

[16] D.A. Woodside, J. Math. Phys. 40 (10) (1999) 4911.

[17] R. Degenhardt, M. Berz, High accuracy description of the fringe fields of particle spectrographs, in: Proceedings 1993 Particle Accelerator Conference, Washington, DC, 1993.

[18] M. Berz, Forward algorithms for high orders and many variables, Automatic Differentiation of Algorithms: Theory, Implementation and Application, SIAM, Philadelphia, 1991.

[19] M. Berz, K. Joh, J.A. Nolen, B.M. Sherrill, A.F. Zeller, Phys. Rev. C 47 (2) (1993) 537.

[20] V.A. Shchepunov, A. Cunsolo, F. Cappuzzello, A. Foti, A. Lazzaro, A.L. Melita, C. Nociforo, J.S. Winfield, Nucl. Instr. and Meth. B 204 (2003) 447.

[21] A. Lazzaro, A. Cunsolo, F. Cappuzzello, A. Foti, C. Nociforo, S. Orrigo, V. Shchepunov, J.S. Winfield, M. Allia, Computational aspects of the trajectory reconstruction in the MAGNEX large acceptance spectrometer, in: Berz, Makino (Eds.), Computational Accelerator Physics 2002, Institute of Physics Conference Series, vol. 175, 2004.

[22] A. Cunsolo, F. Cappuzzello, A.V. Belozyorov, A. Elanique, A. Foti, A. Lazzaro, O. Malishev, L. Melita, W. Mittig, C. Nociforo, P. Roussel-Chomaz, V. Shchepunov, D. Vinciguerra, A. Yeremin, J.S. Winfield, Nucl. Condens. Matter Phys. 513 (1) (2000) 270.

[23] I. Vasserman, S. Sasaki, Comparison of different magnetic measurement techniques, in: Proceedings of 13th International Magnetic Measurement Workshop, 2003.

[24] S.I. Redin, N.M. Ryskulov, G.V. Fedotovich, B.I. Khazin, G.M. Bunce, G.T. Danby, J.W. Jackson, W.M. Morse, R. Prigl, Y.K. Semertzidis, et al., Nucl. Instr. and Meth. A 473 (3) (2001) 260.

[25] K.N. Henrichsen, Overview of magnet measurement methods, in: CERN Accelerator School 1997, 1997.